Numerical Heat Transfer, Part B, 44: 553–574, 2003

ISSN: 1040-7790 print/1521-0626 online
DOI: 10.1080/10407790390231815

A VARIABLE-DENSITY PROJECTION METHOD FOR INTERFACIAL FLOWS

Ming-Jiu Ni and Mohamed Abdou
UCLA MAE Department, Los Angeles, California, USA

Satoru Komori
Department of Mechanical Engineering, Kyoto University, Kyoto, Japan

General second-order, variable-density, three-step and four-step projection methods are developed to simulate unsteady incompressible interfacial flows. A high-accuracy, variable-density RKCN projection method is presented, in which the three-stage, low-storage Runge-Kutta technique and second-order semi-implicit Crank-Nicholson technique are employed to temporally update the convective and diffusion terms, respectively. To reduce computation cost, a simplified version of the projection method is also presented, in which the pressure Poisson equation (PPE) is solved only at the last substage. The level set approach is employed to implicitly capture the interface for falling droplet flows. Three-dimensional bubble rising flows and two-dimensional falling droplet flows in a small closed channel are studied numerically via the present method. By the definition of the effective pressure, the flow mechanisms for falling droplet flows with different density ratios, viscosity ratios, Weber numbers, and Reynolds numbers are discussed.

1. INTRODUCTION

The numerical simulation of interfacial flows is of great importance in investigating the transport phenomena appearing in environmental, geophysical, and industrial flows. Interfacial flow involves the study of not only hydrodynamics in a single phase, but also the interface of two or more immiscible and miscible fluids. Hence the variable-density, incompressible unsteady Navier-Stokes equation needs to be simulated. As for the numerical methods for unsteady, variable-density incompressible Navier-Stokes equations, the variable-density BCG method [1, 18] is often employed for the simulation of interfacial flows, in which the Godunov scheme is used to update the convective term. Kothe and Mjolsness [10] conducted the computation of interfacial flows by the MAC method, in which the explicit updating

Received 17 January 2003; accepted 16 May 2003.
Ming-Jiu Ni acknowledges financial support from the Japan Society for the Promotion of Science (JSPS).
Address correspondence to Ming-Jiu Ni, UCLA MAE Department, 43-133 Engineering IV, Los Angeles, CA 90095-1597, USA. E-mail: mingjiu@fusion.ucla.edu

of the convective and diffusion terms is not stable with a big time-step size. Chen et al. [4] employed the SIMPLE method [25] for the numerical simulation of bubble rising flows. Son and Dhir [19] employed the projection method to do numerical simulation of boiling heat transfer, which incorporates the level set approach for capturing the interface. The first-order fully explicit and full implicit schemes are employed to update the convective and diffusion terms, respectively. The temporal accuracy of the schemes in [4] and [19] has only first order. Ni et al. [14] developed a general four-step or three-step projection method for unsteady incompressible single-phase flows. Also, a RKCN four-step projection method was presented in [14], in which the three-stage, low-storage Runge-Kutta and second-order semi-implicit Crank-Nicholson techniques are employed to update the convective and diffusion terms, respectively. In this article, the general projection method and RKCN projection method for single-phase unsteady incompressible flows will be extended to solve variable-density incompressible interfacial flows. The variable-density RKCN projection method will be simplified further. In the simplified version, the pressure Poisson equation (PPE) will be solved only at the last substage, which will save greatly on computational cost.

Employing the variable-density projection method and the level set method to simulate immiscible interfacial flows in this article, the physical models and numerical algorithms are presented in Section 2. The 3-D rising bubble flows, 2-D falling droplet flows in a small size channel, with different density ratios, viscosity ratios, Reynolds numbers, and Weber numbers are studied numerically in Section 3. Also studied are the mechanisms involved in the deformation and motion of droplets and bubbles. Conclusions are presented in Section 4.

2. PHYSICAL MODELS AND NUMERICAL ALGORITHMS

2.1. Governing Equations

The level set method [16] is employed to capture the interface implicitly by introducing a smooth level set function ϕ, with the zero level set as the interface and positive value outside the interface and negative value inside the interface. Considering the following equation:

$$\frac{\partial \phi}{\partial t} + v \cdot \nabla \phi = 0 \tag{1}$$

which will evolve the zero level of $\phi = 0$ exactly as the actual interface moves. The physical variants can be expressed as

$$\rho = \begin{cases} \rho_1 & \text{if} \quad \phi > 0 \\ \rho_2 & \text{if} \quad \phi < 0 \\ 0.5(\rho_2 + \rho_1) & \text{if} \quad \phi = 0 \end{cases} \qquad \mu = \begin{cases} \mu_1 & \text{if} \quad \phi > 0 \\ \mu_2 & \text{if} \quad \phi < 0 \\ 0.5(\mu_2 + \mu_1) & \text{if} \quad \phi = 0 \end{cases} \tag{2}$$

To keep the level set function as a distance function from the front, an approach based on solving the hyperbolic partial differential equation has been presented in [23]. The reinitialization equation is

$$\phi_t = \text{sign}_\varepsilon(\phi_0)(1 - |\nabla \phi|) \tag{3}$$

$$\phi(\bar{x}, 0) = \phi_0(\bar{x}) \tag{4}$$

where $|\nabla\phi| = \sqrt{\phi_x^2 + \phi_y^2 + \phi_z^2}$, and the sign function $\mathrm{sign}_\varepsilon(\phi_0) = 2\left[H_\varepsilon(\phi_0) - \frac{1}{2}\right]$ with the Heaviside function $H_\varepsilon(\phi)$ defined as

$$H_\varepsilon(\phi) = \begin{cases} 0 & \text{if} \quad \phi < -\varepsilon \\ \dfrac{1}{2}\left[1 + \dfrac{\phi}{\varepsilon} - \dfrac{1}{\pi}\sin\left(\dfrac{\pi\phi}{\varepsilon}\right)\right] & \text{if} \quad |\phi| \le \varepsilon \\ 1 & \text{if} \quad \phi > \varepsilon \end{cases}$$

Since the level set function is a smooth function, Eq. (1) can be easily solved numerically by employing a high-resolution discretization scheme for the convective term.

A continuum surface force (CSF) model [2, 3] is used to reformulate the surface tension as a volume force $\bar{F}_{sv}$. For the level set approach, we have the formulation of the CSF model as $\bar{F}_{SV} = k(\phi)\,\delta_\varepsilon(\phi)\,\nabla\phi$ with the surface tension delta function $\delta_\varepsilon(\phi) = \partial H_\varepsilon(\phi)/\partial\phi$ and the front curvature $k(\phi) = \nabla\cdot(\nabla\phi/|\nabla\phi|)$. By employing the CSF model for the surface tension force and a level set approach to capture the interface, we have the governing equations for an incompressible interfacial flow as

$$\nabla\cdot v = 0 \tag{5}$$

$$\frac{\partial v}{\partial t} + \nabla\cdot(vv) = -\frac{1}{\bar{\rho}}\nabla p + \frac{1}{\bar{\rho}\mathrm{Re}}\nabla\cdot(\bar{\mu}\nabla v) + s \tag{6}$$

$$\frac{\partial\phi}{\partial t} + v\cdot\nabla\phi = 0 \tag{7}$$

$$s = -\frac{g}{\mathrm{Fr}} - \frac{k(\phi)\,\delta_\varepsilon(\phi)\,\nabla\phi}{\bar{\rho}\,\mathrm{We}} + \frac{1}{\bar{\rho}\mathrm{Re}}\nabla\cdot\left[\bar{\mu}(\nabla v)^T\right] \tag{8}$$

with dimensionless groups of Reynolds, Froude, and Weber numbers as $\mathrm{Re} = \rho_1 LU/\mu_1$, $\mathrm{Fr} = U^2/gL$, $\mathrm{We} = \rho_1 LU^2/\sigma$, respectively; $\bar{\mu} = \mu/\mu_1$ and $\bar{\rho} = \rho/\rho_1$ are the dimensionless ratios of the viscosity and density, respectively. Here U, L are characteristic velocity and length, respectively, σ is the surface tension coefficient, while μ_i, ρ_i $(i = 1, 2)$ are viscosity coefficients and densities of fluid 1 and fluid 2, respectively. For simplicity, hereafter we will instead use $\bar{\mu}$ and $\bar{\rho}$ with μ and ρ, respectively. To prevent instability, it is necessary to smooth the values of the density ρ and viscosity μ as

$$\rho_\varepsilon(\phi) = \lambda_\rho + (1 - \lambda_\rho)H_\varepsilon(\phi) \tag{9}$$

$$\mu_\varepsilon(\phi) = \lambda_\mu + (1 - \lambda_\mu)H_\varepsilon(\phi) \tag{10}$$

where $\lambda_\rho = \rho_2/\rho_1$ and $\lambda_\mu = \mu_2/\mu_1$.

2.2. Time-Integration–Variable-Density Projection Method

A general second-order projection method has been presented in [14] for incompressible Navier-Stokes equations. Considering the variable-density,

incompressible Navier-Stokes eqautions (5) and (6), we have the following general second-order, variable, four-step projection method as

$$A\hat{v} = r - \frac{\nabla p^n}{\rho^{n+1/2}} \tag{11}$$

$$\tilde{v} = \hat{v} + \alpha\,\Delta t\,\frac{\nabla p^n}{\rho^{n+1/2}} \tag{12}$$

$$\alpha\,\Delta t\,\nabla\cdot\left(\frac{\nabla p^{n+1}}{\rho^{n+1/2}}\right) = \nabla\cdot\tilde{v} \tag{13}$$

$$v^{n+1} = \tilde{v} - \alpha\,\Delta t\,\frac{\nabla p^{n+1}}{\rho^{n+1/2}} \tag{14}$$

and three-step projection method as

$$A\hat{v} = r - \frac{\nabla p^n}{\rho^{n+1/2}} \tag{15}$$

$$\alpha\,\Delta t\,\nabla\cdot\left[\frac{\nabla\left(p^{n+1} - p^n\right)}{\rho^{n+1/2}}\right] = \nabla\cdot\hat{v} \tag{16}$$

$$v^{n+1} = \hat{v} - \alpha\,\Delta t\,\frac{\nabla(p^{n+1} - p^n)}{\rho^{n+1/2}} \tag{17}$$

For the trapezoidal method, we have $\alpha = \frac{1}{2}$. Here A is a submatrix, and the right-hand-side r vector contains all those quantities that are already known. Different updating techniques for the convective and diffusion terms will produce different formulations of A or r. For example, when Crank-Nicholson and explicit techniques are employed for the updating of the diffusion term and the convective term respectively, we have A and r as follows:

$$A = \frac{1}{\Delta t}\left[I - \frac{\Delta t}{2\,\mathrm{Re}}\,\frac{1}{\rho^{n+1/2}}\nabla\cdot(\mu^{n+1/2}\nabla)\right] \tag{18}$$

$$r = \frac{1}{\Delta t}\left[I + \frac{\Delta t}{2\,\mathrm{Re}}\,\frac{1}{\rho^{n+1/2}}\nabla\cdot(\mu^{n+1/2}\nabla)\right]v^n - \nabla\cdot(vv)^{n+1/2} \tag{19}$$

where I is the unit identity matrix operator. It is apparent that Eqs. (11)–(14) and Eqs. (15)–(17) are second-order approximations to Eqs. (5) and (6) with error term as

$$\frac{(\Delta t^2)}{2\mathrm{Re}}\nabla\cdot\left\{\mu^{n+1/2}\nabla\left[\frac{1}{\rho^{n+1/2}}\nabla\left(\frac{p^{n+1} - p^n}{\Delta t}\right)\right]\right\}$$

Usually, we can employ an explicit updating technique for the convective term for simplicity. However, due to the weak stability of the Adams-Bashforth scheme, Choi and Moin [5] employed the semi-implicit Crank-Nicholson technique

to update both the convective and the diffusion terms. The general four-step projection method (11)–(14) will form the variable-density Choi-Moin method with $\alpha = 1$ by employing the Crank-Nicholson scheme for the convective and diffusion terms. It should be noted that the implicit updating of the convective term does not favor the implementation of higher-order spatial schemes. The second-order central difference scheme is utilized to conduct the spatial discretization of the convective term in the original Choi-Moin method for incompressible Navier-Stokes equation.

The second-order-accuracy Dukowicz-Dvinsky method [6] is often employed to do the direct numerical simulation (DNS) of incompressible turbulent flows. It needs to solve the Poisson equation of pressure difference. In fact, the general three-step projection method of (15)–(17) with $\alpha = \frac{1}{2}$ forms the variable-density Dukowicz-Dvinsky projection method for the variable-density incompressible Navier-Stokes equation. The original second-order Dukowicz-Dvinsky method was designed for solving the Stokes flow, in which the Crank-Nicholson scheme was employed to update the diffusion term with good stability. The projection method (15)–(17) with $\alpha = 1$ was also employed to simulate the boiling heat transfer [19] incorporated with the level set approach, in which the first-order fully implicit scheme and the explicit scheme were employed to update the diffusion and convective terms respectively.

The Bell-Marcus method [1] can also be written in the form of Eqs. (15)–(17), with Godunov updating and Crank-Nicholson updating for the convective and diffusion terms, respectively. Usually, the Godunov scheme has only second-order spatial accuracy. The variable-density Bell-Colella-Glaz has been employed by many researchers [1, 18] to do multifluid flows, since the robust Godunov scheme is employed for the updating of the convective term.

The RKCN high-accuracy projection method developed in [14] for single-phase incompressible flow has second-order temporal accuracy, in which three-stage Runge-Kutta technique and second-order semi-implicit Crank-Nicholson technique have been employed to update the convective and diffusion terms, respectively. Here we extend the method to the variable-density unsteady incompressible Navier-Stokes equations, incorporating with a level set equation for the interfacial flows. The variable-density RKCN projection method can be expressed as

$$A^m \hat{v}^m = r^m - \frac{\alpha^m \nabla p^{m-1} + \beta^m \nabla p^{m-2}}{\rho^{n+1/2}} \tag{20}$$

$$\tilde{v}^m = \hat{v}^m + \Delta t \frac{\alpha^m \nabla p^{m-1} + \beta^m \nabla p^{m-2}}{\rho^{n+1/2}} \tag{21}$$

$$\alpha^m \nabla \cdot \left(\frac{\nabla p^m}{\rho^{n+1/2}} \right) = \frac{1}{\Delta t} \nabla \cdot \tilde{v}^m - \beta^m \nabla \cdot \left(\frac{\nabla p^{m-1}}{\rho^{n+1/2}} \right) \tag{22}$$

$$v^m = \tilde{v}^m - \Delta t \left(\frac{\alpha^m \nabla p^m + \beta^m \nabla p^{m-1}}{\rho^{n+1/2}} \right) \tag{23}$$

$$\phi^{m+1} = \phi^m - \Delta t (\alpha^{m+1} v^m \cdot \nabla \phi^m + \beta^{m+1} v^{m-1} \cdot \nabla \phi^{m-1}) \tag{24}$$

where

$$A^m = \frac{1}{\Delta t}\left[1 - \frac{\gamma^m \Delta t}{\rho^{n+1/2}\,\mathrm{Re}}\nabla\cdot(\mu^{n+1/2}\nabla)\right] \tag{25}$$

$$r^m = \frac{1}{\Delta t}\left[1 + \frac{\gamma^m \Delta t}{\mathrm{Re}\,\rho^{n+1/2}}\nabla\cdot(\mu^{n+1/2}\nabla)\right]v^{m-1} - \alpha^m[S]^{m-1} - \beta^m[S]^{m-2} \tag{26}$$

$S = s - \nabla\cdot(vv)$ and $\alpha^m = \left\langle \frac{8}{15}, \frac{5}{12}, \frac{3}{4}\right\rangle$, $\beta^m = \left\langle 0, -\frac{17}{60}, -\frac{5}{12}\right\rangle$ and $\gamma^m = \left\langle \frac{4}{15}, \frac{1}{15}, \frac{1}{6}\right\rangle$. The velocity components and pressure in the intermediate velocities equation at the first substep are $u_i^{-1} = 0$, $p^{-1} = 0$ $(m-2=-1)$ and $u_i^0 = u_i^n$, $p^0 = p^n$ $(m-1=0)$. At the third step, they are $u_i^3 = u_i^{n+1}$ and $p^3 = p^{n+1}$, which are the updated velocities and pressure for the next time level, $n+1$. The density and viscosity are updated using ϕ^{n+1}, which will be the $\rho^{n+1/2}$, $\mu^{n+1/2}$ at the next time step.

In the above variable-density RKCN projection method, the Crank-Nicholson implicit technique is employed to update the diffusion term for stability and the low-storage three-stage Runge-Kutta technique is employed to update the convective term for simplicity and stability. The projection method also has second-order temporal accuracy for variable-density unsteady incompressible flows. The diffusion term can be spatially discretized using standard central difference schemes. The convective term in the momentum equation can be conveniently updated using the second-order CD scheme or high-order compact schemes [11] or fully conservative high-order accuracy schemes as developed in [13]. To improve the stability and resolution, we discretize the convective term in Eq. (24) for the level set function by employing the second-order TVD scheme and higher-order ENO scheme. For the discretized equations of Eqs. (20)–(26), we employ the following formulas for the density and viscosity at the central points of the control volumes and the interpolation values at the cell surfaces as

$$\rho_i = \lambda_\rho + (1-\lambda_\rho)H_\varepsilon(\phi_i)\mu_i = \lambda_\mu + (1-\lambda_\mu)H_\varepsilon(\phi_i) \tag{27}$$

$$\frac{1}{\rho_{i+\frac{1}{2}}} = 0.5\left(\frac{1}{\rho_i} + \frac{1}{\rho_{i+1}}\right)\frac{1}{\mu_{i+1/2}} = 0.5\left(\frac{1}{\mu_i} + \frac{1}{\mu_{i+1}}\right) \tag{28}$$

For the variable-density RKCN projection method, the PPE needs to be solved at every stage, which will consume much more time. To save computing time, Le and Moin [11] presented a simplified version for a Runge-Kutta–type fractional-step method. Here we also present the simplified version for the above variable-density RKCN projection method as

$$A^m\hat{v}^m = r^m - \frac{(\alpha^m + \beta^m)\nabla p^n}{\rho^{n+1/2}} \tag{29}$$

$$\tilde{v}^m = \hat{v}^m + \Delta t\frac{(\alpha^m + \beta^m)\nabla p^n}{\rho^{n+1/2}} \tag{30}$$

$$v^m = \tilde{v}^m - \Delta t\frac{(\alpha^m + \beta^m)\sum_{l=1}^{m}(\alpha^l + \beta^l)\nabla p^n}{\rho^{n+1/2}} \qquad \text{for } m = 1, 2 \tag{31}$$

$$v^3 = \tilde{v}^3 - \Delta t \frac{\sum_{l=1}^{3} (\alpha^l + \beta^l) \nabla p^{n+1}}{\rho^{n+1/2}} \qquad \text{for } m = 3 \tag{32}$$

$$\nabla \cdot \left[\frac{\sum_{l=1}^{3} (\alpha^l + \beta^l) \nabla p^{n+1}}{\rho^{n+1/2}} \right] = \frac{1}{\Delta t} \nabla \cdot \tilde{v}^3 \tag{33}$$

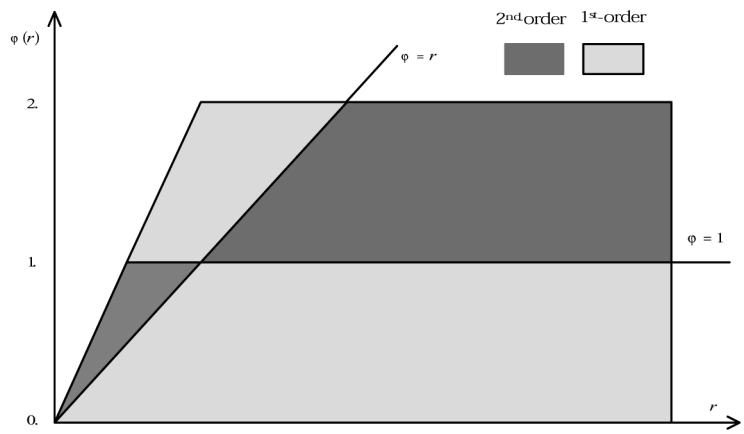

(a) 1st- and 2nd-order TVD region in [23]

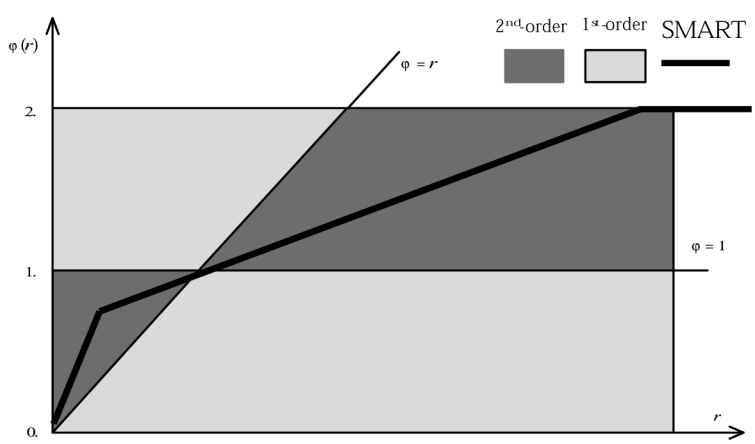

(b) 1st- and 2nd-order TVD region in this paper

Figure 1. Regions of TVD discretization for the convective term.

$$\phi^{m+1} = \phi^m - \Delta t(\alpha^{m+1} v^m \cdot \nabla\phi^m + \beta^{m+1} v^{m-1} \cdot \nabla\phi^{m-1}) \tag{34}$$

where A_i^m and r_i^m have the same formulas as in Eqs. (25) and (26). For the simplified version of the variable-density RKCN projection method, the PPE needs to be solved only at the last substage. This will save considerable computation time. Usually the simplified version has second-order temporal accuracy, like the original one. To accelerate the convergence and to enforce the divergence-free velocity, the four-level multigrid technique has been employed to solve the discretized PPE for both the variable-density RKCN projection method and its simplified version.

2.3. Reinitialization for Level Set Function

In general, even if the level set function ϕ is initialized as a signed distance from the interface front, it will not remain a distance function at later time. For large time computations, keeping the level set function as a distance function will be advantageous in the computation of surface tension, which is difficult to compute near a steep gradient in the distance function. In the meantime, the distance function of ϕ will ensure that the front has a finite thickness for all time, and the values for $\rho(\phi)$ will not be greatly distorted with $\nabla\phi$ equal to one. Sussman et al. [22] presented the reinitialization equation as Eqs. (3) and (4), which can be reformulated as

$$\phi_t + w \cdot \nabla\phi = \mathrm{sign}_\varepsilon(\phi_0) \tag{35}$$

where

$$w = \mathrm{sign}_\varepsilon(\phi_0)\frac{\nabla\phi}{|\nabla\phi|} \tag{36}$$

For level set approaches, another important issue is mass conservation. We know the total mass is conserved in time for an incompressible flow. Theoretically, the solution ϕ of Eqs. (35) and (36) will have the same sign and the same zero level set as ϕ_0, which means the interface will not move with time marching for the solution of Eqs. (35) and (36). Away from the interface, ϕ will converge to $|\nabla\phi| = 1$. Therefore it will converge to the actual distance. The unmoved interface with $|\nabla\phi| = 1$ will ensure total mass conservation. However, the numerical discretization of the reinitialization equation of the level set function will not preserve the property in general. Hou et al. [9] have found that a considerable amount of total mass is lost in time by the above reinitialization of the level set function. To ensure mass conservation, a method similar to that in [22] has been employed to ensure mass conservation.

2.4. TVD and ENO Schemes for the Convective Term of the Interfacial Evolving Equation

To improve stability and resolution, we discretize the convective terms for the level set function and its reinitialization equation by employing the SMART [7] and ENO schemes [20]. The SMART scheme is in fact a second-order TVD scheme [15], although it is not included in the TVD region of Sweby [23]. In [15], the extended TVD region is presented, which is shown in Figure 1*b*, while Sweby's region is shown

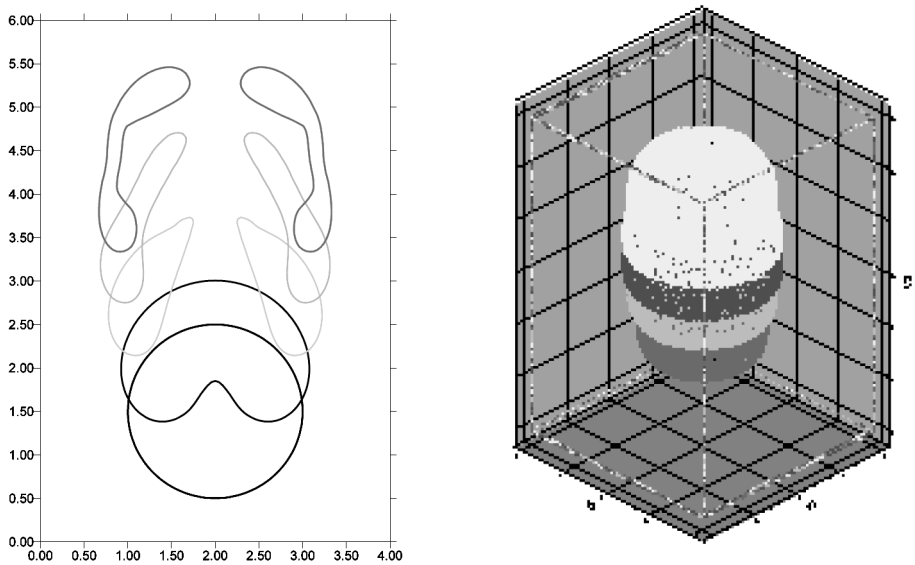

Figure 2. Evolving 3-D shape of rising bubble for Re = 100, We = 500, density ratio = 0.0125, viscosity ratio = 0.0125.

in Figure 1*a*. In the figure, φ is a function of r with $r_i = \Delta\phi_{i-1}/\Delta\phi_i$, which is a limiter to construct the TVD scheme. When $\varphi = r$ and $\varphi = 1$, we have the second-order upwind difference scheme and the central difference scheme, respectively. The SMART scheme is also shown on the Figure 1*b*.

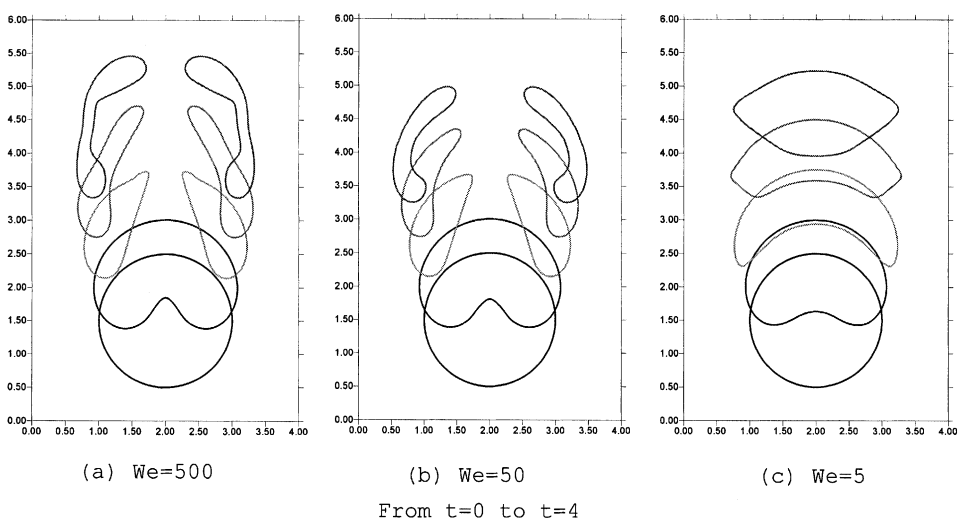

Figure 3. Effect of surface tension on the rising bubble for Re = 100, density ratio = 0.0125, viscosity ratio = 0.0125.

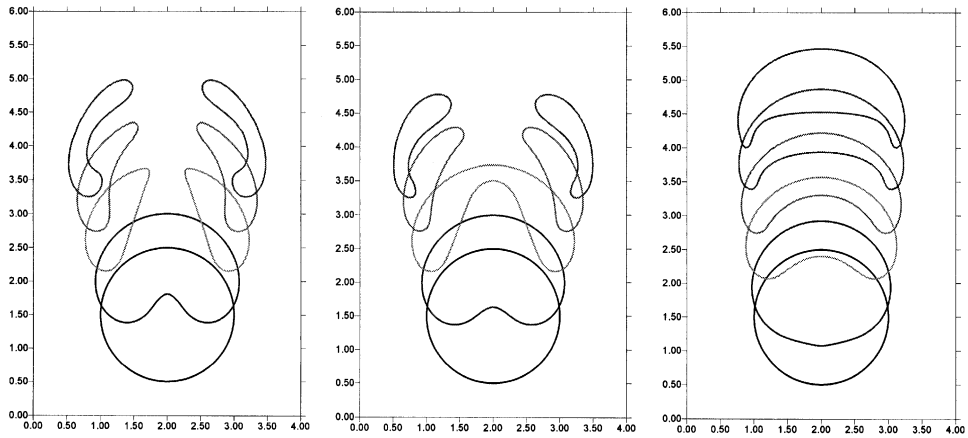

(a) Re=100 From t=0 to t=4 (b) Re=50 From t=0 to t=4 (c) Re=10 From t=0 to t=5

Figure 4. Effect of viscous force on the rising bubble for We = 50, density ratio = 0.0125, viscosity ratio = 0.0125.

3. SIMULATION OF RISING BUBBLE AND FALLING DROPLET FLOWS

3.1. Rising Bubble Flows and Code Validation

The rise and deformation of 3-D bubbles in a liquid with initial bubble radius R_0 are simulated by the above-developed methods. The nondimensional governing equation is formulated as in Eqs. (5)–(8) with dimensionless groups of Reynolds, Froude, and Weber numbers as $\mathrm{Re} = \rho_1 g^{1/2} R_0^{3/2}/\mu_1$, $\mathrm{Fr} = 1$, and $\mathrm{We} = \rho_1 g R_0^2/\sigma$

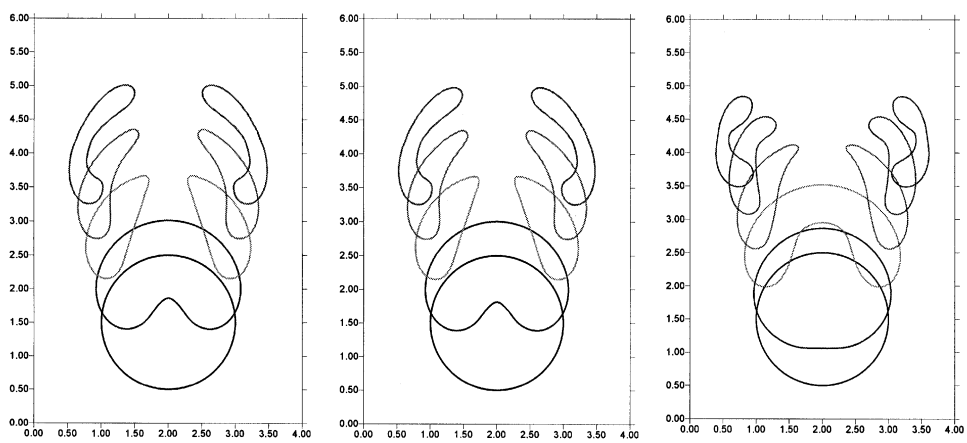

(a) Density Ratio=0.001 From t=0 to t=4 (b) Density Ratio=0.01 From t=0 to t=4 (c).Density Ratio=0.2 From t=0 to t=5

Figure 5. Effect of density ratio on the rising bubble for Re = 100, We = 50, viscosity ratio = 0.0125.

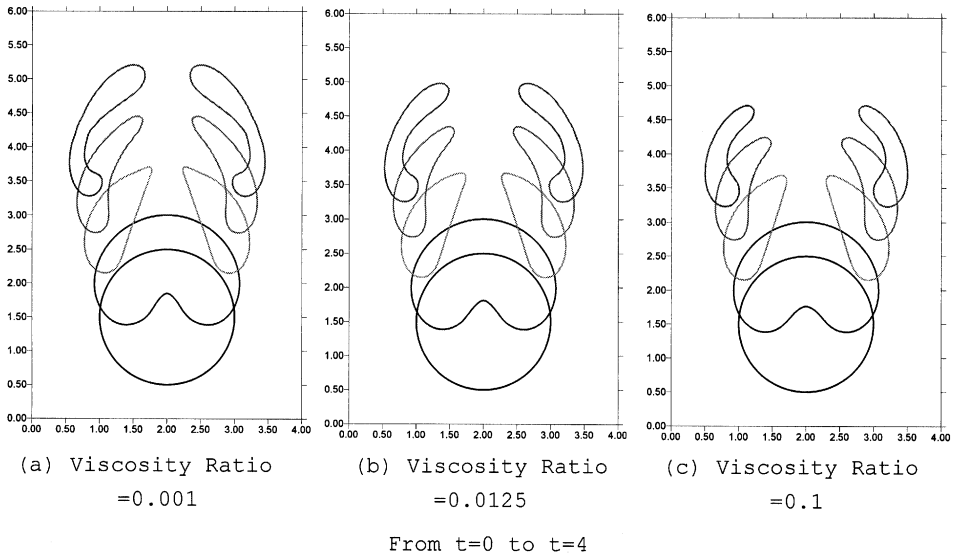

Figure 6. Effect of viscosity ratio on the rising bubble for Re = 100, We = 50, density ratio = 0.0125.

after defining the characteristic velocity and length as $U = (gR_0)^{1/2}$ and $L = R_0$, respectively. Driven by the buoyancy force, the bubble rises.

In a 3-D rectangle channel with free-surface boundary on the top and nonslip walls on the other sides, an initially stationary spherical bubble is considered with the initial condition $u_i(t = 0) = 0$ and boundary conditions $u_3 = 0$, $\partial u_i/\partial x = 0$ $(i = 1, 2)$ on the top surface, and $u_i = 0$ on the solid walls. The computation is performed using the simplified variable-density RKCN projection method and the level set method. The reinitialization equation has been solved with the variable time-step size method to keep the total mass conservative for this method. The $65 \times 65 \times 97$ meshes are utilized for the rising bubble flow in a rectangular channel with $4R_0$ width, $4R_0$ length, and $6R_0$ depth. Here R_0 is the initial sphere bubble radius. The four-level multigrid technique is employed for the solution of the PPE to enforce divergence-free velocity. For this computation, the maximum residue of the velocity divergence in every computational cell is kept less than 10^{-6}.

The numerical results in a 3-D rectangular channel are similar to the results in a cylindrical channel [4]. The shape development of the bubble rising in a liquid with a density ratio of $\lambda_\rho = \rho_g/\rho_l = 0.0125$ is shown as a set of superimposed calculations in Figure 2.

The effects of surface tension and viscous force on the bubble dynamics can be investigated by changing the values of the Weber number and Reynolds number, respectively. Here the role of surface tension in the formation of a toroidal bubble has been studied with Weber numbers 5, 50, and 500, while the Reynolds number, density ratio, and viscosity ratio are kept as constants (Re = 100, $\lambda_\rho = \rho_g/\rho_l = 0.0125$, $\lambda_\mu = \mu_g/\mu_l = 0.0125$). For the case of the lowest Weber number (We = 5) in Figure 3*c*, the water jet formed below the bubble is unable to penetrating the upper surface and an elliptical bubble forms owing to the high surface tension. With a decrease of the surface tension for the cases of We = 50 and 500 in Figure 3*b* and

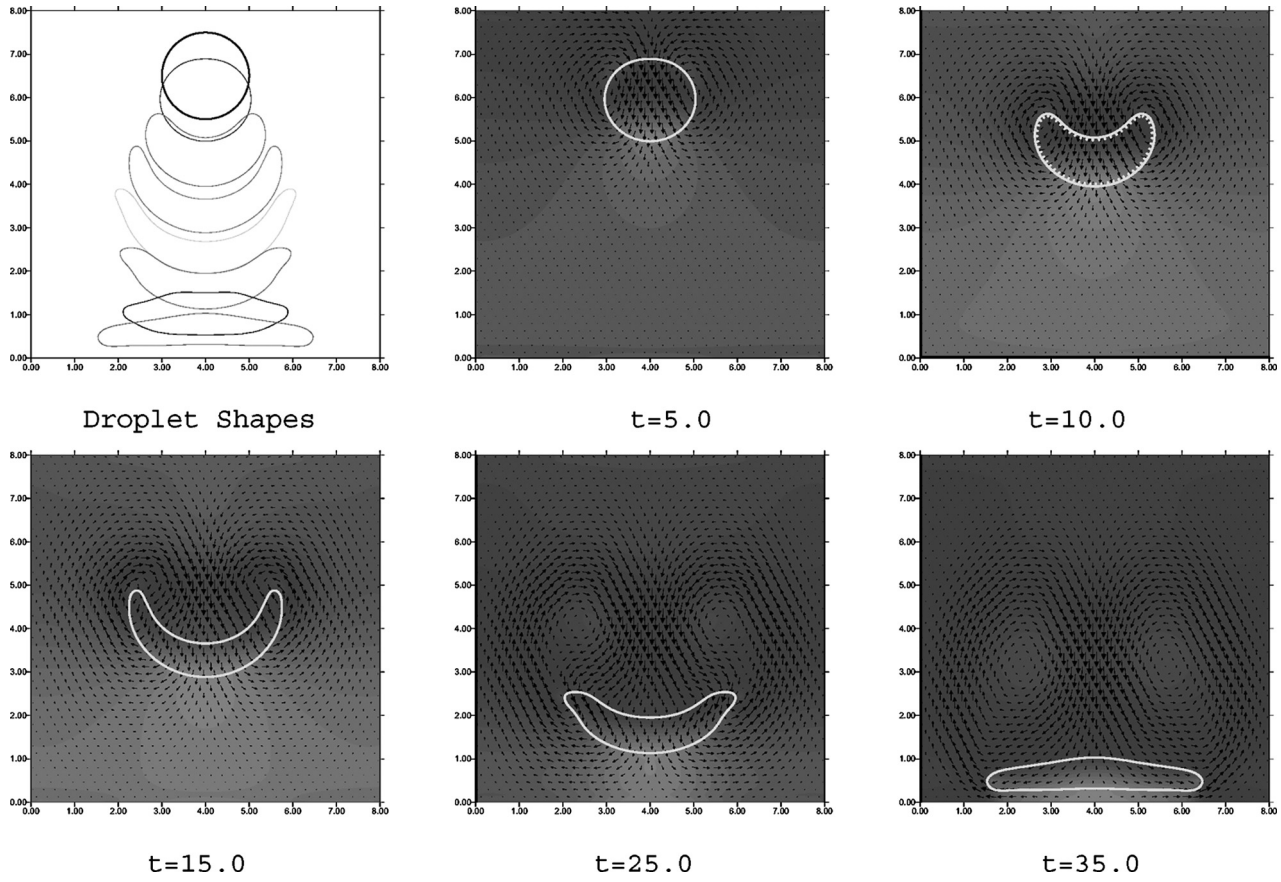

Figure 7. Droplet evolution shapes and velocity vector distribution from $t = 5.0$ to $t = 35.0$ for $\mathrm{Re} = 100$, $\mathrm{We} = 50$, viscosity ratio $= 1.0125$, density ratio $= 1.125$.

Figure 3*a*, the toroidal bubble does form eventually. Near the upper boundary the bubble velocity will be reduced due to the restriction of the boundary condition of $u_3 = 0.0$, which can be regarded as the wall repulsion effect.

Figure 4 illustrates the effect of the viscous force on the motion of the bubble. For the low Reynolds number flow of $\mathrm{Re} = 10$, due to the big effect of the viscous force, the liquid jet below the bubble is very weak and the bubble rises as a cap. At increased Reynolds number $\mathrm{Re} = 50$, the effect of the buoyancy is much greater than the effect of the viscous force, and the jet motion drives the lower surface to pierce the upper surface, forming a toroid.

An increase in the density ratio leads to an increase of the net force of the difference between the buoyancy force and gravity, which will result in a higher upward bubble velocity. The effect of density ratio and viscosity ratio on the bubble deformation and motion are also shown in Figures 5 and 6. All of the above results are consistent with the results in [4]. It is reasonable to believe that the present code and methods can be applied to study the droplet deformation and motion mechanisms in a liquid.

3.2. Falling Droplet Flows in a Small Closed Channel

The falling and deformation of a droplet in a liquid with initial droplet radius R_0 are simulated. The droplet falls driven by the gravity. In a 2-D rectangle closed channel, an initially stationary circle droplet is considered with initial central at point (4.0, 6.5) and radius 1.0. The initial velocity condition is set as $u_i(t = 0) = 0$, and boundary condition $u_i = 0$ is set on the solid walls. The computation is finished using the simplified variable-density RKCN projection method incorporating the level set method. The reinitialization equation has been solved by the variable time-step size method to keep the level set function as a distance function from the front and to ensure overall mass conservation. A collocated grid system with the meshes of 65×65 is utilized to do the numerical simulation of falling droplet flows in a liquid. The four-level V-type multigrid technique is employed to enforce the divergence-free velocity. For this computation, the maximum residue of the velocity divergence in every computational cell is kept less than 10^{-6}.

3.2.1. The falling and deformation mechanisms of a droplet in a liquid. For the 1.125 density ratio flow, Figure 7 illustrates that the droplet begins to fall owing to gravity force. For the sake of analysis, the velocity vector and contours of the effective pressure $p' = p - \rho g h$ (h is the distance from the top wall) have been shown in Figure 7. The static hydropressure $\rho g h$ has been deduced from the original pressure p. In fact, the static hydropressure will produce an upward buoyancy. However, due to the 1.125 density ratio (which is greater than 1), the net force of the gravity force and the static buoyancy on the droplet is downward. In Figure 7, the black row line shows the velocity vector distribution, while the red filling color shows the high-effective-pressure region and the blue filling color shows the low-effective-pressure region. When the droplet begins to fall, the effective pressure on the lower surface of the droplet is higher than that on its upper surface. The difference between the effective pressure on the lower and upper surfaces will develop a vortex on the both sides of the droplet, which has a sense of rotation (Figure 7 at $t = 5.0$).

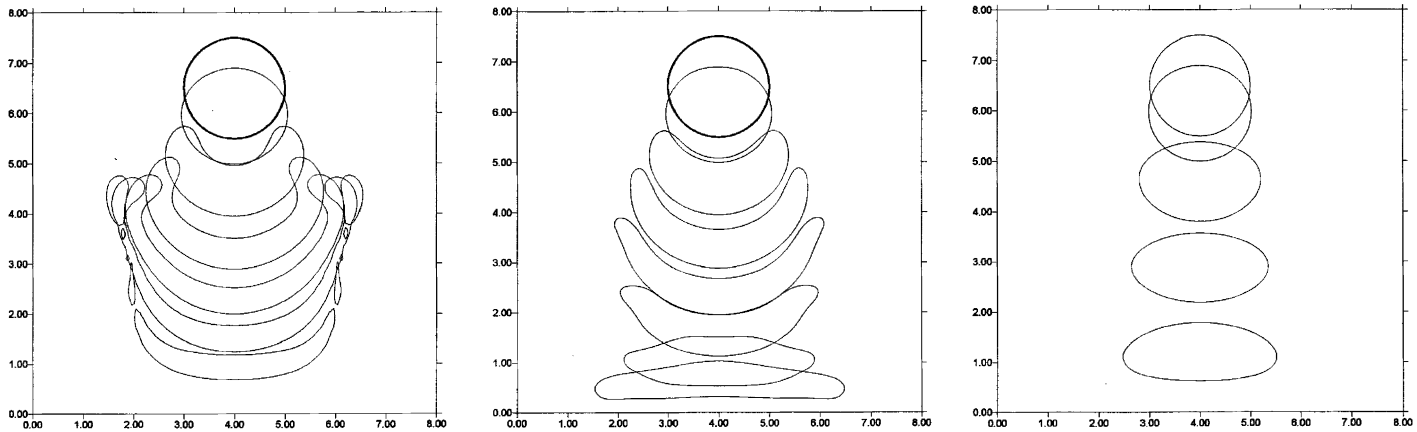

(a) We=500
from t=0 to t=30

(b) We=50
from t=0 to t=35

(c) We=5
from t=0 to t=20

Figure 8. Effect of surface tension for the case of Re = 100, density ratio = 1.125, viscosity ratio = 1.0125.

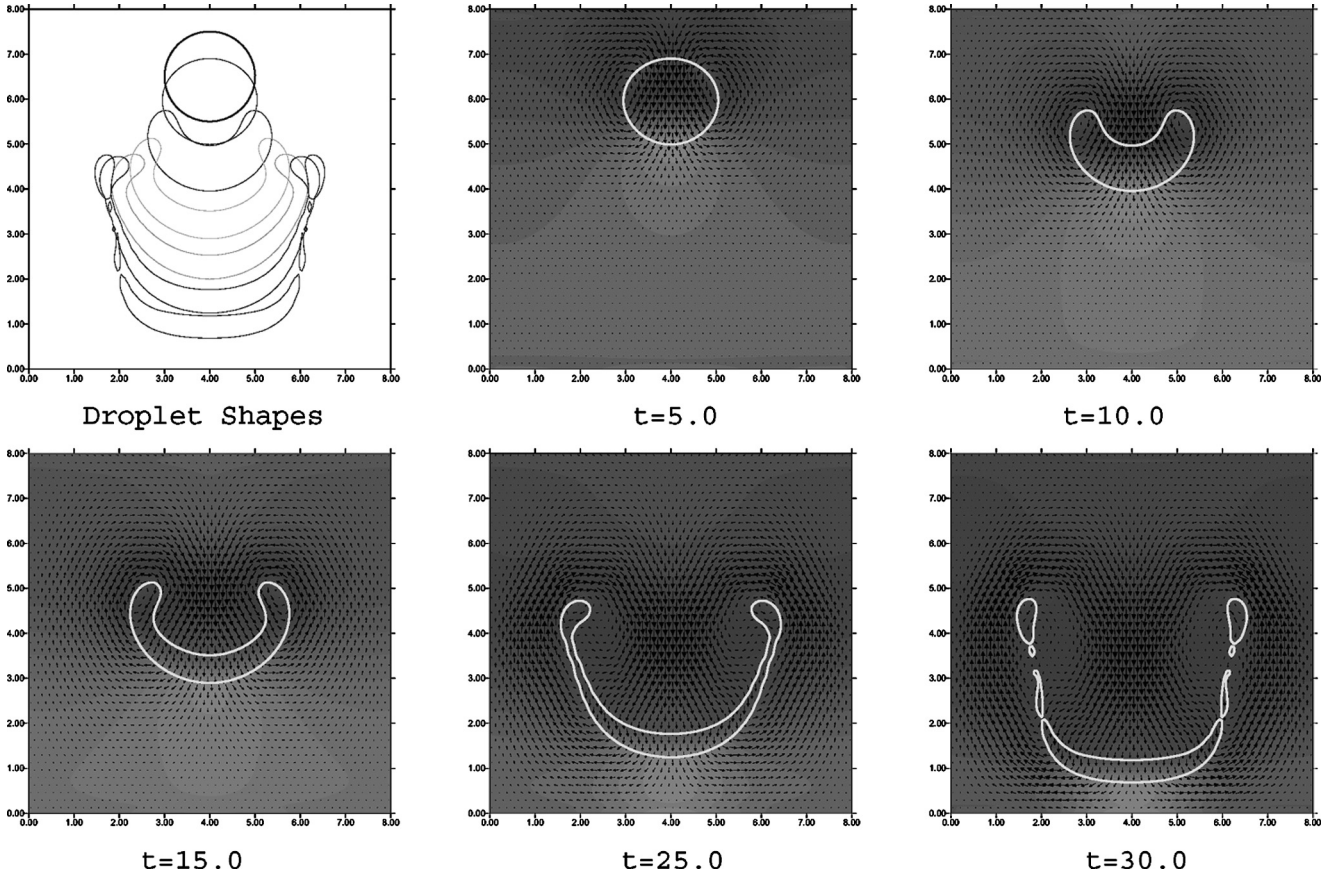

Figure 9. Droplet evolution shapes and velocity vector distribution for Re = 100, We = 500, viscosity ratio = 1.0125, density ratio = 1.125.

The vortex induces the motion of a jet, which pushes the liquid into the droplet from above, as may be seen in Figure 7 at $t = 5.0$ and $t = 10.0$. The vortex center is also the lowest-effective-pressure region.

Due to the effect of the jet, a velocity difference is formed between the top surface and the lower surface. The velocity difference results in the top surface approaching the lower surface, as may be seen at $t = 15.0$ and $t = 20.0$ in Figure 7. When the droplet is close to the wall, a high effective pressure is formed between the lower surface of the droplet and the wall, which will block the movement of the droplet toward to the bottom wall, as shown at $t = 25.0$ in Figure 7. The two horns of the deformed droplet move toward the two sides owing to the rotation of the two low-pressure vortexes, which will increase the effect of wall repulsion as shown at $t = 35.0$, and the falling velocity of the droplet will be reduced.

3.2.2. The role of surface tension in the deformation of a falling droplet. From Eqs. (4) and (6), the effect of surface tension on the droplet dynamics can be investigated by changing the value of the Weber number. Here the role of surface tension in the deformation of a droplet has been studied with Weber numbers 5, 50, and 500, while the Reynolds number and the ratios of density and viscosity are kept constant (Re = 100, viscosity ratio = 1.0125, density ratio = 1.125). Figure 8 illustrates the effect of surface tension on the development of the droplet. For the lowest Weber number (Figure 8*c*, We = 5), owing to the high surface tension, a higher-effective-pressure region is formed inside the droplet. The water jet formed above the droplet is unable to penetrate the lower surface and an elliptical droplet forms. As the droplet approaches the wall, due to the wall repulsion (high effective pressure formed between the lower surface of the droplet and the wall), the ratio of the long axis to the short axis becomes larger. We cannot see the two horns on the sides of the droplet which are formed for the case of We = 50 in Figure 8*b*. For We = 500, the large effective pressure difference between the lower surface and the top surface will form a strong jet, which induces a large velocity difference between the top and lower surfaces (Figure 9 at $t = 5.0$ and $t = 10.0$). Due to the large velocity difference, the top surface approaches the lower surface (Figure 9 at $t = 10.0$, $t = 15.0$, and $t = 25.0$), and it finally pierces the lower surface and several droplets are formed (Figure 9 at $t = 30.0$). This is the result for 2-D case. For the 3-D case, high Weber number flow will produce a toroidal droplet. The droplet shape evolution for We = 5, 50, and 500 is shown in Figure 8. It shows clearly that the primary effect of surface tension is to resist the deformation of the falling droplets.

3.2.3. The role of Reynolds number in the deformation of a falling droplet. The effect of viscous force on the motion of the droplet can also be investigated by varying the Reynolds number while the other flow parameters are kept constant. Here we do the computation for the cases of We = 50, viscosity ratio = 1.0125, density ratio = 1.125, with Reynolds numbers 5, 25, and 100. For the lowest Reynolds number flow of Re = 5, due to the large effect of the viscous force, the liquid jet formed on the droplet is very weak and the droplet falls down as an elliptical shape (as shown in Figure 10*c*). With increase of the Reynolds number to Re = 100, the effect of the net force of gravity force and buoyancy is much greater than the effect of the viscous force. The strong jet formed on the droplet

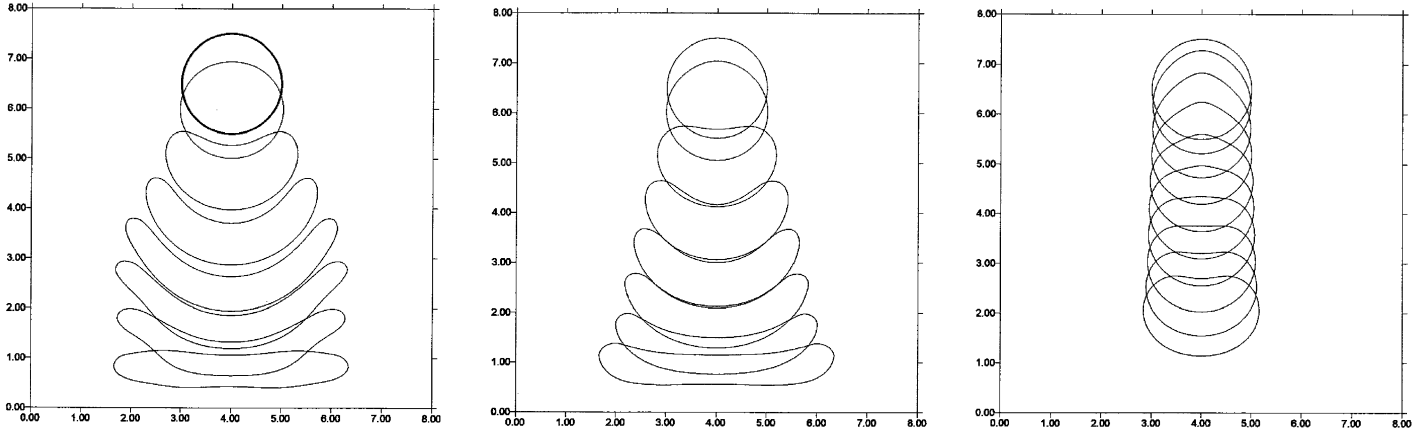

(a) Re=100
from t=0 to t=35

(b) Re=25
from t=0 to t=35

(c) Re=5
from t=0 to t=40

Figure 10. Effect of viscous force for the case of We = 50, density ratio = 1.1250, viscosity ratio = 1.0125.

surface drives the upper surface to approach the lower surface and form the horn shapes at $t = 15.0$ in Figure 10*a*. At $t = 35.0$, due to the wall repulsion, the horn shape becomes flat. It is expected that the stronger jet will induce a much larger velocity difference between the top and low surfaces of the droplet when the Reynolds number is much higher, and the droplet will be split into several small droplets.

3.2.4. The role of viscosity ratio in the deformation of a falling droplet. To study the effect of the viscosity ratio on the deformation and movement of the falling droplets in a closed channel, values of the viscosity ratio 1.0125, 5.0, and 50.0 have been employed, while Reynolds number, Webers number, and density ratio are kept constant, with $\mathrm{Re} = 100$, $\mathrm{We} = 50$, and density ratio $= 1.125$, respectively. The computation results are shown in Figure 11.

For the case of low viscosity ratio (1.0125 in Figure 11*a*), we find the droplet deformation is much larger than the deformation for the case of large viscosity ratio (50 in Figure 11*c*). In fact, due to the high viscosity ratio, the effective pressure inside the droplet is much larger than that outside the droplet, which will resist the deformation of the droplet. The deformation for the case of 5.0 viscosity ratio in Figure 11*b* is in the middle of the deformation of 1.0125 and 50 viscosity ratios.

3.2.5. The role of density ratio in the deformation of a falling droplet. An increase in the density ratio leads to an increase of the net force of the difference between the gravity and buoyancy force, which will result in a higher falling velocity for the droplet, which can be seen in Figure 12. The falling velocity of droplet for density ratio 1.250 (Figure 12*a*) is apparently larger than that for density ratio 1.050 (Figure 12*c*). Also, we find the deformation in Figure 12*a* is larger than the deformation in Figure 12*b*, since a greater net force will form a stronger jet upper the top surface of the droplet.

4. SUMMARY AND CONCLUSION

General second-order, four-step and three-step, variable-density projection methods have been presented to simulate the unsteady, variable-density incompressible Navier-Stokes equations, and a high-order, variable-density RKCN projection method has been presented based on the general four-step, variable-density projection method, in which the three-stage, low-storage Runge-Kutta and second-order semi-implicit Crank-Nicholson techniques are employed to update the convective and diffusion terms for simplicity and stability, respectively. Especially, a simplified version of the projection method has also been developed for variable-density interfacial flows. In the simplified version, the PPE needs to be solved only at the last substage, which saves much computational cost. The four-level multigrid technique has been employed to enforce divergence-free velocity for incompressible flows. The hyperbolic equation for the level set function has been incorporated to capture the interface automatically with high accuracy. The 3-D rising bubble flows and 2-D falling droplet flows with a variation of density ratio, Weber and Reynolds numbers, and viscosity ratios have been simulated. The effective pressure distribution, velocity vector distribution, and vortex are shown to analyze the droplet falling

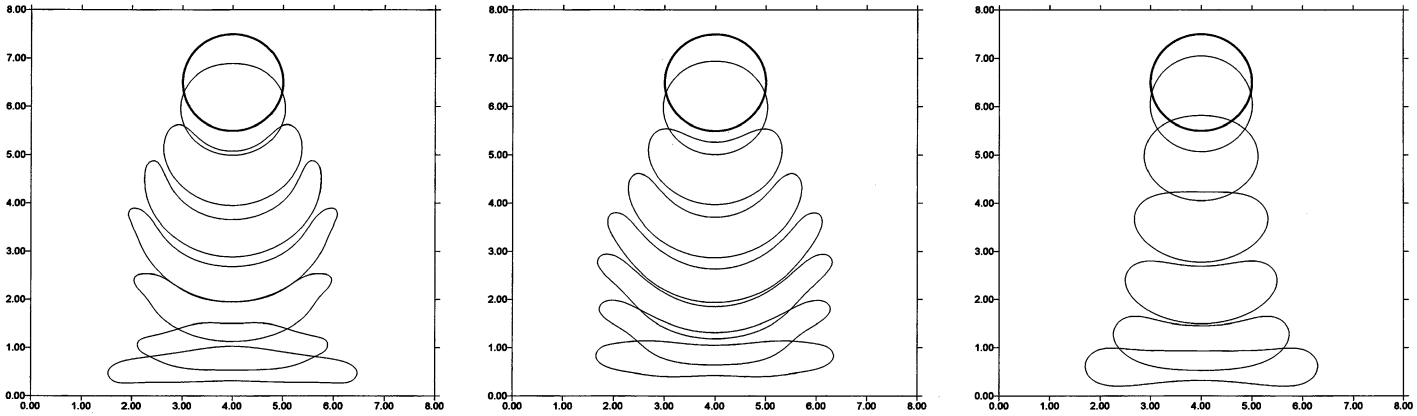

(a) Viscosity Ratio=1.0125 from t=0 to t=35

(b) Viscosity Ratio=5.0 from t=0 to t=35

(c) Viscosity Ratio=50.0 from t=0 to t=30

Figure 11. Effect of viscosity ratio for the case of Re = 100, We = 50, viscosity ratio = 1.0125.

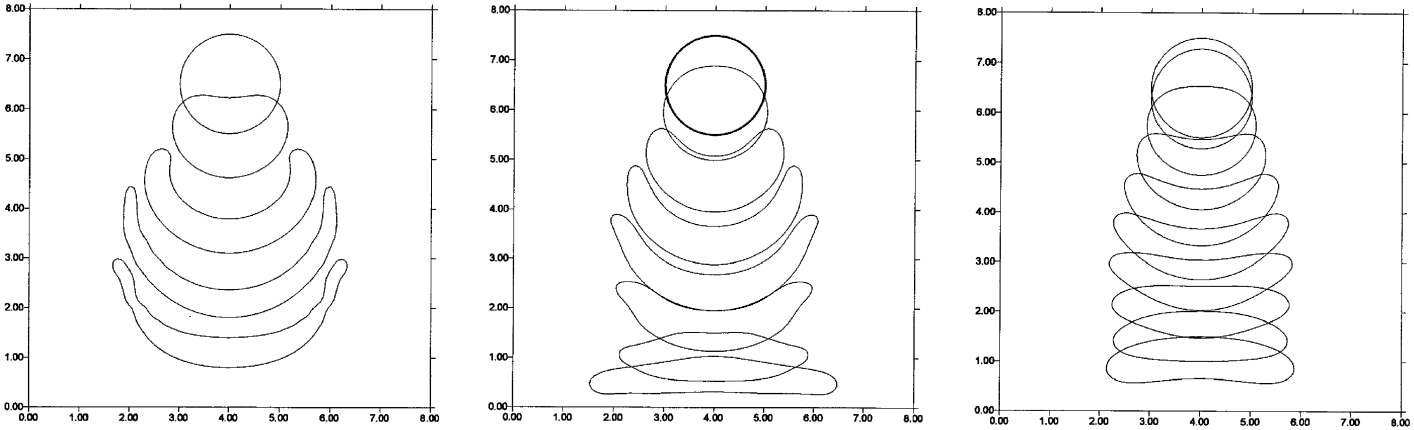

(a) Density Ratio=1.250 from t=0 to t=20

(b) Density Ratio=1.125 from t=0 to t=35

(c) Density Ratio=1.050 from t=0 to t=45

Figure 12. Effect of density ratio for the case of Re = 100, We = 50, density ratio = 1.1250.

and deformation mechanisms for the flow in a closed channel. It has been shown that the Weber number, Reynolds number, viscosity, and density ratios have a big effect on droplet deformation.

REFERENCES

1. J. B. Bell and D. L. Marcus, A Second-Order Projection Method for Variable Density Flows, *J. Comput. Phys.*, vol. 101, p. 334, 1992.
2. J. U. Brackbill, D. B. Kothe, and C. Zemach, A Continuum Method for Modeling Surface Tension, *J. Comput. Phys.*, vol. 100, no. 2, pp. 335–354, 1992.
3. Y. C. Chang, T. Y. Hou, B. Merriman, and S. Osher, A Level Set Formulation of Eulerian Interface Capturing Methods for Incompressible Fluid Flows, *J. Comput. Phys.*, vol. 124, pp. 449–464, 1996.
4. L. Chen, S. V. Garimella, J. A. Reizes, and E. Leonardi, The Development of a Bubble Rising in a Viscous Liquid, *J. Fluid Mech.*, vol. 387, pp. 61–96, 1999.
5. H. Choi and P. Moin, Effects of the Computational Time Step on Numerical Solutions of Turbulent Flow, *J. Comput. Phys.*, vol. 113, pp. 1–4, 1994.
6. J. K. Dukowicz and A. S. Dvinsky, Approximation Factorization as a High Order Splitting for Implicit Incompressible Flow Equations, *J. Comput. Phys.*, vol. 102, pp. 336–347, 1992.
7. P. H. Gaskell and A. K. C. Lau, Curvature Compensated Transport SMART, A New Boundedness Preserving Transport Algorithm, *Int. J. Numer. Meth. Fluids*, vol. 8, pp. 617–641, 1988.
8. F. H. Harlow and J. E. Welch, Numerical Calculation of Time-Dependent Viscous Incompressible Flow of Fluid with Free Surface, *Phys. Fluids*, vol. 8, no. 12, pp. 2182–2189, 1965.
9. T. Y. Hou, P. Rosakis, and P. LeFloch, A Level-Set Approach to the Computation of Twinning and Phase-Transition Dynamics, *J. Comput. Phys.*, vol. 150, pp. 302–331, 1999.
10. D. B. Kothe and R. C. Mjolsness, RIPPLE: A New Model for Incompressible Flows with Free Surfaces, *AIAA J.*, vol. 30, no. 11, pp. 2694–2700, 1992.
11. H. Le and P. Moin, An Improvement of Fractional Step Methods for Incompressible Navier-Stokes Equations, *J. Comput. Phys.*, vol. 92, pp. 369–379, 1991.
12. S. K. Lele, Compact Finite Difference Schemes with Spectral-Like Resolution, *J. Comput. Phys.*, vol. 103, pp. 16–42, 1992.
13. Y. Morinishi, T. Lund, O. V. Vasilyev, and P. Moin, Fully Conservative Higher Order Finite Difference Schemes for Incompressible Flow, *J. Comp. Phys.*, vol. 143, pp. 90–124, 1998.
14. M.-J. Ni, S. Komori, and N. Morley, Projection Methods for the Calculation of Incompressible Unsteady Flows, *Numer. Heat Transfer B*, vol. 44, pp. 533–551, 2003.
15. M.-J. Ni, Development of Difference Schemes and the Application of Finite Volume Method in Simulation of Turbulent Flow Field in Centrifugal Compressors, Ph.D. thesis, Xi'an Jiaotong University, China, 1997.
16. S. Osher and J. A. Sethin, Fronts Propagating with Curvature-Dependent Speed: Algorithms Based on Hamilton-Jacobi Formulations, *J. Comput. Phys.*, vol. 79, no. 1, pp. 12, 1988.
17. S. V. Patankar, *Numerical Heat Transfer and Fluid Flow*, McGraw-Hill, New York, 1980.
18. E. G. Pucket, A. S. Almgren, J. B. Bell, D. L. Marcus, and W. J. Rider, A High-Order Projection Method for Tracking Fluid Interfaces in Variable Density Incompressible Flows, *J. Comput. Phys.,* vol. 143, pp. 90–124, 1997.
19. G. Son and V. K. Dhir, Numerical Simulation of Saturated Film Boiling on a Horizontal Surface, *ASME J. Heat Transfer*, vol. 119, pp. 525–533, 1997.

20. C.-W. Shu and S. Osher, Efficient Implement of Essential Non-oscillatory Shock-Capturing Schemes, II, *J. Comput. Phys.*, vol. 83, pp. 32–78, 1989.
21. M. Sussman and E. Fatemi, An Efficient, Interface Preserving Level Set Redistancing Algorithm and Its Application to Interfacial Incompressible Flow, *SIAM J. Sci. Comput.,* vol. 20, pp. 1165–1191, 1999.
22. M. Sussman, P. Smereka, and S. Osher, A Level Set Approach for Computing Solutions to Incompressible Two-Phase Flow, *J. Comput. Phys.*, vol. 114, pp. 146–159, 1994.
23. P. K. Sweby, High Resolution Schemes Using Flux Limiters for Hyperbolic Conservation Laws, *SIAM J. Numer. Anal.*, vol. 21, no. 5, 1984.